

Effect of Nb on Magnetic Properties, Microstructures, and Site Preference in Nd-Fe-B Nanograin Single-Phase Alloy

Fang Yang¹ · Lei-chen Guo² · Guang-le Dong³ · Yan-li Sui³ · Ping Qian⁴ · Zhi-meng Guo¹ · Ping Li¹

Received: 21 February 2016 / Accepted: 22 April 2016 / Published online: 6 June 2016
© Springer Science+Business Media New York 2016

Abstract The effect of Nb addition on the magnetic properties, microstructure, and site preference has been investigated in single-phase $\text{Nd}_{12.3}\text{Fe}_{81.7-x}\text{Nb}_x\text{B}_{6.0}$ ($x = 0\text{--}3.0$) alloy ribbons. Those ribbons were treated by subsequent annealing. The optimum magnetic properties with $J_r = 0.94$ T, $H_{ci} = 919.0$ kA/m, and $(\text{BH})_{\text{max}} = 143.1$ kJ/m³ were achieved by annealing the melt-spun ribbons with $x = 1.5$ at 650 °C for 10 min. Additions of Nb were effective in refining the grain size and improving the magnetic properties. Transmission electron microscopy (TEM) showed that there was no second phase or precipitate found in grain boundaries. The results of three-dimensional atom probe (3DAP) indicated that Nb may enter into the amorphous structure and $\text{Nd}_2\text{Fe}_{14}\text{B}$. The content of Nb in $\text{Nd}_2\text{Fe}_{14}\text{B}$ was very small. Theoretical calculation showed that Nb preferentially substituted Fe atoms at the $8j_2$ sites and the volume of a cell would slightly enlarge.

Keywords Magnetic properties · Microstructure · Site preference · 3DAP

✉ Guo Zhimeng
guozhimengustb@163.com

- ¹ Institute for Advanced Materials and Technology, University of Science and Technology Beijing, Beijing 100083, China
- ² School of Engineering Technology, Purdue University, West Lafayette, IN, 47907-2021, USA
- ³ State Key Laboratory for Advanced Metals and Materials, University of Science and Technology Beijing, Beijing 100083, China
- ⁴ Institute of Applied Physics, University of Science and Technology, Beijing 100083, China

1 Introduction

As the rare earth permanent magnets of the third generation, Nd-Fe-B magnets have been extensively studied in respect to their industrial applications [1]. To improve their magnetic properties, extensive efforts have been made by the substitution of other elements [2–5]. Nb is the most commonly used. The effect of its addition on nanocomposite magnets was reported by some researchers [6–8]. The result showed that the addition of Nb can improve the thermal stability of amorphous phase and the energy product of nanocomposites [6, 7]. Proper addition of Nb could inhibit the formation of TbCu_7 -type metastable phase, which would be decomposed into $\text{Nd}_2\text{Fe}_{14}\text{B}$ and a-Fe phase [8].

For the site preference of Nb, different views exist. Yamasaki et al. [9] reported that Nb hardly enters a-Fe or $\text{Nd}_2\text{Fe}_{14}\text{B}$ phase and that Nb and B atoms were enriched in the remaining amorphous phase, inhibiting grain growth. Chen et al. [10] reported that Nb preferably segregates at grain boundaries to form Nb-rich intergranular phase rather than entering the $\text{Pr}_2\text{Fe}_{14}\text{B}$ matrix, indicating that Nb does not enter the 2:14:1 phase. Wang et al. [11, 12] studied the influence of Nb on $(\text{Nd}_{0.9}\text{Dy}_{0.1})_{9.5}\text{Fe}_{79-x}\text{Co}_5\text{Nb}_x\text{B}_{6.5}$ ($x = 0, 1, 5$) alloy. They reported that with 1 % Nb addition, Nb atoms were enriched in the boundary phase [11], while the ratio of Nb, Fe, and B atoms in Nb-enriched boundary phase reaches 1:1:1, and more Nb atoms were found in $\text{Nd}_2\text{Fe}_{14}\text{B}$ phase [12]. Wang et al. [13] studied the site preference of Nb in $\text{Nd}_2\text{Fe}_{14}\text{B}$ by using interatomic pair potentials. They believed that Nb atoms were inclined to enter $\text{Nd}_2\text{Fe}_{14}\text{B}$ and replace Fe in the j_2 site. However, the effect of Nb substitution on the $\text{Nd}_2\text{Fe}_{14}\text{B}$ single-phase nanograin alloy has not been understood well, especially its role in microstructure and site preference. Therefore, the

alloys of $\text{Nd}_{12.3}\text{Fe}_{81.7-x}\text{Nb}_x\text{B}_{6.0}$ ($x = 0-3.0$) with different Nb content were studied in this work, focusing on the magnetic properties, microstructure, and site preference.

2 Experiment

2.1 Experimental Method

The $\text{Nd}_{12.3}\text{Fe}_{81.7-x}\text{Nb}_x\text{B}_{6.0}$ ($x = 0, 0.5, 1.0, 1.5, 2.0, 2.5, 3.0$) alloy ingots were obtained by applying the melt-spinning technique to a wheel at a speed of 22 and 30 m/s. The ribbon samples with a width of 2–3 mm and a thickness of 40–50 μm were isothermally annealed in the range of 550–800 $^{\circ}\text{C}$ for 10 min in vacuum-sealed quartz tubes to crystallize. Phase analysis of the samples was characterized by X-ray diffractometer with $\text{Cu-K}\alpha$ radiation. Magnetic measurement at room temperature was employed using a LDJ9600 vibrating sample magnetometer (VSM). The length direction of the ribbons was parallel to the applied field in order to minimize demagnetization effect. The microstructures were observed by high-resolution transmission electron microscopy (HR-TEM JEM2010) with thin foils prepared by ion-beam thinning. A three-dimensional atom probe (3DAP) was employed to investigate the elemental distribution at a near-atomic resolution.

2.2 Computational Method

At the beginning of the 1980s, Carlsson [14] reported that the cohesive energy of a metal could be obtained by an ab initio method and that the pair potentials could be inverted from the calculated cohesive energy curves. Using this method, interatomic potentials can be constructed. In the middle of 1990s, Chen's inversion theorem was developed. It is a rigorous and concise approach to obtain the interatomic pair potential based on the cohesive energy curves [15, 16]. The interatomic pair potentials were obtained by Chen's lattice inversion in detail [17–19]. The pair potentials were fitted simply by the Morse function

$$\varphi(x) = D_0 \left\{ e^{[-r(\frac{x}{R_0}-1)]} - 2e^{[-(\frac{r}{2})(\frac{x}{R_0}-1)]} \right\} \quad (1)$$

where D_0 and R_0 are potential parameters. The other parameters are shown in Fig. 1.

3 Result and Discussion

3.1 Phase Analysis and Magnetic Properties

Figure 2 shows the XRD patterns of melt-spun $\text{Nd}_{12.3}\text{Fe}_{81.7-x}\text{Nb}_x\text{B}_{6.0}$ ($x = 0, 1.0, 2.5$). At the spinning

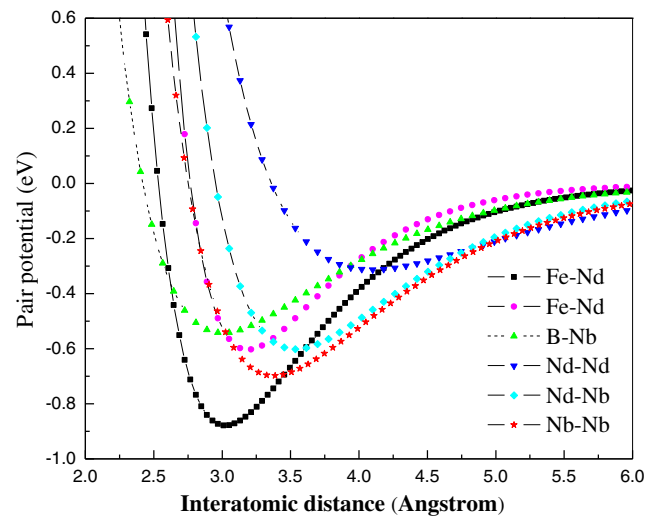


Fig. 1 The other important interatomic potentials

speed of 22 m/s, the addition of 2.5 % Nb also revealed the relatively weak crystallization peak. Comparing Fig. 2a with Fig. 2b, as the spinning speed increases, diffraction peak intensity decreases and the amorphous forming ability is improved. The ribbons with $x = 0$ were not a completely amorphous phase and the obvious characteristic peaks of $\text{Nd}_2\text{Fe}_{14}\text{B}$ emerged. When $x = 1$, the melt-spun ribbons were almost completely amorphous alloy. While the melt-spun ribbons with $x = 2.5$ were completely amorphous, a typical characteristic of amorphous state—the diffuse scattering peaks in the XRD—already existed. It suggested that Nb addition improved the ability of the alloy to form an amorphous alloy and inhibited the formation of crystalline phase at the speed of 30 m/s. The contrary crystallization

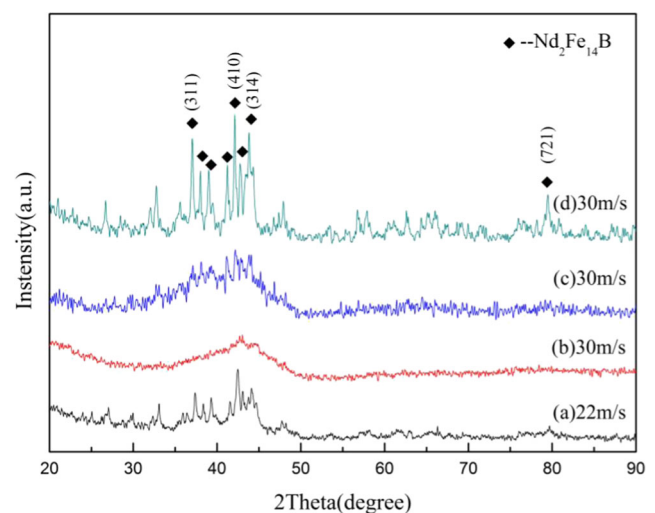


Fig. 2 XRD plots of melt-spun $\text{Nd}_{12.3}\text{Fe}_{81.7-x}\text{Nb}_x\text{B}_{6.0}$ ribbons with spinning the speed of 22 and 30 m/s. (a) $x = 2.5$, (b) $x = 2.5$, (c) $x = 0$, (d) $x = 1$

Table 1 Optimal magnetic properties of Nd_{12.3}Fe_{81.7-x}Nb_xB_{6.0} at different experiment conditions

Nb (at %)	(BH) _{max} (kJ/m ³)	H _{ci} (kA/m)	J _r (T)	J _r /J _s	Annealing condition
0.5	141.09	867.94	1.02	0.73	600 °C 10 min
1.0	125.61	908.08	0.90	0.73	650 °C 10 min
1.5	143.12	918.96	0.94	0.73	650 °C 10 min
2.0	139.62	980.67	0.96	0.75	650 °C 10 min
2.5	118.13	1200.0	0.87	0.72	650 °C 10 min
3.0	116.61	1085.11	0.84	0.74	650 °C 10 min

phenomenon with the crystallization tendency improved as a result of the Mn substitution in Nd₉Fe_{85-x}Mn_xB₆ ($x = 0, 0.5, 1$) was observed by Xie et al. [19].

Many literatures [7, 20, 21] on this issue has shown that nanocomposite or single-phase Nd₂Fe₁₄B exhibits the best properties between 550 and 800 °C. In order to achieve the best magnetic properties for each alloy, a thermal treatment at a temperature range of 550 to 800 °C for 10 min was employed individually to gain a fine structure. The best magnetic properties of each alloy are listed in Table 1. It can be seen that optimum magnetic properties with (BH)_{max} = 143.1 kJ/m³, J_r = 0.94 T, H_{ci} = 919.0 kA/m are achieved by annealing the melt-spun ribbons with $x = 1.5$ at 650 °C for 10 min. It can be concluded that the exchange coupling effect between the grains in this alloy is stronger, the grain size is small, and the distribution is relatively uniform. Although the content of Nb was different, the high performance of the alloy system appeared at 650 °C for 10 min. The hysteresis loops and magnetic properties of Nd_{12.3}Fe_{81.7-x}Nb_xB_{6.0} ($x = 0.5\sim 3.0$) alloy annealed at 650 °C for 10 min are shown in Fig. 3. It can be seen that the addition of Nb can improve the magnetic properties significantly and the square of the hysteresis

curves is good. As Nb content increased, remanence (J_r) and the maximum magnetic energy product (BH)_{max} were first increased and then decreased. The maximum magnetic energy product was increased first from 123.9 kJ/m³ ($x = 0.5$) to 143.1 kJ/m³ ($x = 1.5$) and then decreased to 116.6 kJ/m³ ($x = 3.0$). All magnetic energy products were larger than 115 kJ/m³. However, the coercive force (H_{ci}) increased as Nb content increased, reaching a peak when $x = 2.5$. When the grain size is reduced to nanometer scale, the properties of magnetic materials can change significantly. Grain size, grain orientation, spatial distribution, intergranular exchange effect, anisotropy field, and other factors in magnetic phase will affect the magnetic properties. As for remanence(J_r), as the grain size decreases, a strong exchange coupling effect between adjacent grains is produced and the remanence enhancement effect is obvious. But when the Nb content exceeds a certain value, the microstructure can change significantly and remanence may decrease, as shown in Fig. 3b. As for the coercive force (H_{ci}), it is the structural sensitivity parameter. As Nb content increases, the grain size of the alloy decreases; as a result, the coercive force increases. The influence of remanence to the maximum magnetic energy product (BH)_{max} is greater

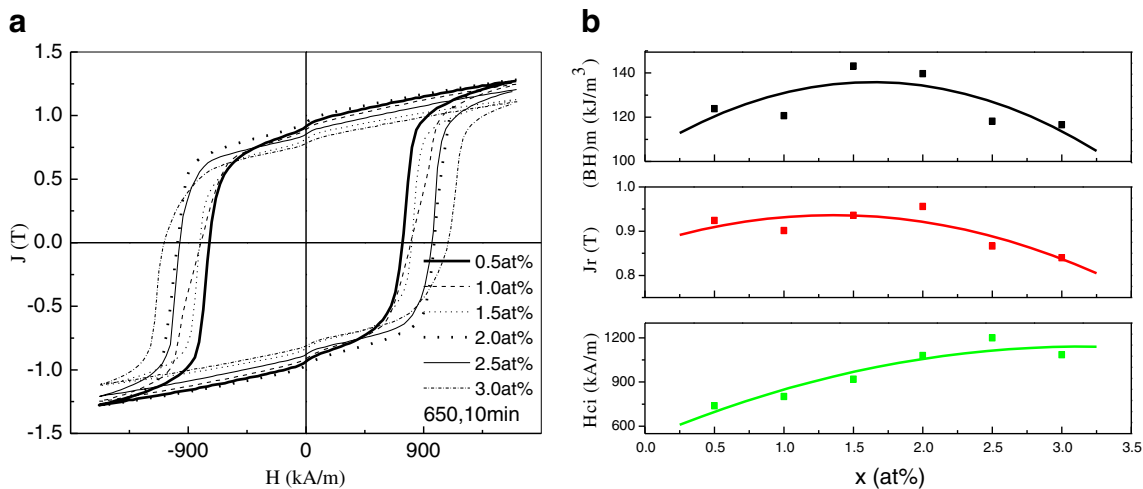
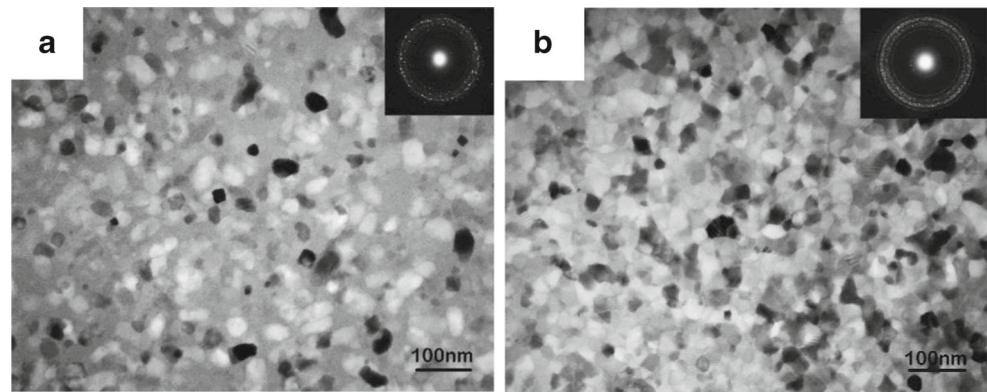


Fig. 3 Hysteresis loop and magnetic properties of the Nd_{12.3}Fe_{81.7-x}Nb_xB_{6.0} ($x = 0.5\sim 3.0$) ribbons annealing at 650 °C for 10 min. **a** Hysteresis loop, **b** magnetic properties

Fig. 4 TEM images of $\text{Nd}_{12.3}\text{Fe}_{79.2}\text{Nb}_{2.5}\text{B}_{6.0}$ ribbons annealed at different temperature for 10 min. **a** 600 °C, **b** 650 °C



than that of the coercive force. With Nb addition, the change of (BH)_{max} is similar to that of remanence.

3.2 Microstructure

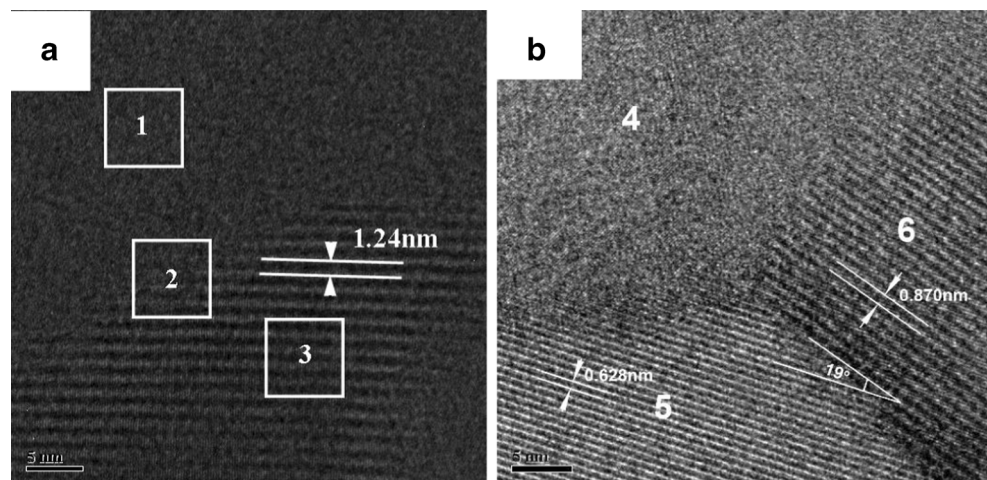
Figure 4 shows the TEM images of $\text{Nd}_{12.3}\text{Fe}_{79.2}\text{Nb}_{2.5}\text{B}_{6.0}$ ribbons annealed at 600 and 650 °C for 10 min, respectively. Comparing the two graphs, it can be found using the selected area analysis that the electron diffraction ring in Fig. 4a is not completely continuous, indicating the presence of the amorphous phase and $\text{Nd}_2\text{Fe}_{14}\text{B}$ crystal phase in the alloy ribbons. The grain size is about 30–40 nm. In Fig. 4b, with the same composition and condition after crystallization at 650 °C for 10 min, the selected electron diffraction ring becomes continuous, indicating that the crystallization of the $\text{Nd}_2\text{Fe}_{14}\text{B}$ phase volume fraction is greatly increased. The grain size is also about 30–40 nm. There is no obvious increase of grain, nearing to complete crystallization.

Figure 5a is a HRTEM image of the $\text{Nd}_{12.3}\text{Fe}_{79.2}\text{Nb}_{2.5}\text{B}_{6.0}$ alloy after annealing at 600 °C for 10 min. The Fourier

filtered images corresponding to different sections of Fig. 5a are shown in Fig. 6. It can be seen that, in Fig. 5a, region 1 of the Fourier transform spectrum has an amorphous characteristic, as is shown in Fig. 6a. Region 2 (Fig. 5a) is a boundary between amorphous zone 1 and crystallization zone 3. Therefore, region 2 is a reflection of region 3 of the diffraction spots and region 1 of amorphous ring superimposition, as shown in Fig. 6b. The Fourier transform spectrum of region 3 (Fig. 5a) is completely characterized, as is shown in Fig. 6c.

Figure 5b shows the HRTEM images of $\text{Nd}_{12.3}\text{Fe}_{79.2}\text{Nb}_{2.5}\text{B}_{6.0}$ alloy annealed at 650 °C for 10 min. In order to further clarify the microstructure and crystallization of the district, the Fourier transform is made, and the Fourier transform spectrum of each region has obvious characteristics of the crystal lattice image. Although the HRTEM image of region 4 (Fig. 5b) is not seen as a regular lattice arrangement, it is known that the crystallization phase is characterized by the Fourier transformation, as is shown in Fig. 6d. By calibrating, this is the orientation $[\bar{1}11]$ of the $\text{Nd}_2\text{Fe}_{14}\text{B}$ phase. In Fig. 5b, the phase angle

Fig. 5 HR-TEM images of $\text{Nd}_{12.3}\text{Fe}_{79.2}\text{Nb}_{2.5}\text{B}_{6.0}$ annealed ribbon. **a** Annealed at 600 °C for 10 min, **b** annealed at 650 °C for 10 min



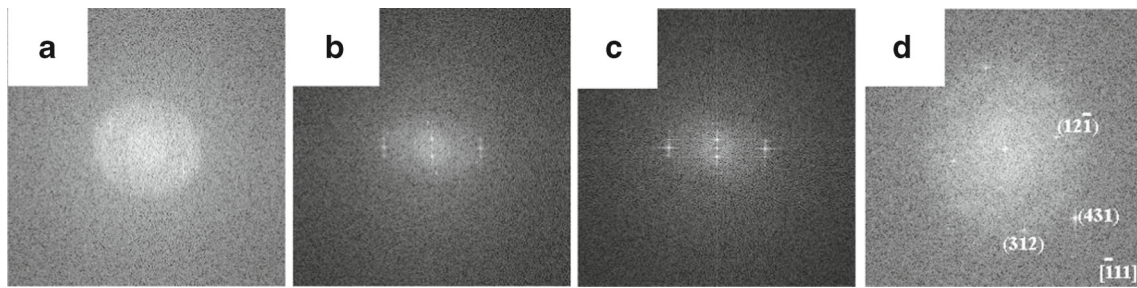


Fig. 6 Fourier filtered images corresponding to different sections in Fig. 5a. **a** Corresponding to Fig. 5a zone 1, **b** corresponding to Fig. 5a zone 2, **c** corresponding to Fig. 5a zone 3, and **d** corresponding to Fig. 5b zone 4

between grain 5 and grain 6 is 19 degrees, which belongs to the large angle grain boundaries. As is shown above, the grain boundary can be divided into two kinds: the amorphous boundary of the $\text{Nd}_2\text{Fe}_{14}\text{B}$ grain and the boundary between $\text{Nd}_2\text{Fe}_{14}\text{B}$ grains. Figure 5a is the first kind of grain boundary. Figure 5b is a reflection of the second kind of grain boundaries. From Fig. 5a and the Fourier transform spectrum, it can be seen that the internal crystallization of the material after annealing at 600 °C for 10 min is not complete. The crystallization of grains in zone 2 is incomplete and the Fourier transform spectrum appears to be an amorphous diffraction ring, which indicates that they are not fully balanced phase. From Fig. 5b, it can be seen that the internal crystallization of the material is complete after annealing at 650 °C for 10 min, which revealed the formation of the boundary between the $\text{Nd}_2\text{Fe}_{14}\text{B}$ grains.

Regardless of the boundary type, there is no second phase or precipitates found in the grain boundaries.

3.3 Site Preference

As-spun ribbons with 2.5 % Nb addition exhibited the characteristic peaks of $\text{Nd}_2\text{Fe}_{14}\text{B}$ at a speed of 22 m/s in Fig. 2. Figure 7 shows the 3DAP analysis results of these ribbons. Nb exhibits periodic ups and downs. It seems that in the grain boundaries where the nanocrystalline Nb atoms have a higher concentration, the Nb-rich region forms. This region hinders the growth of nanograins, therefore impeding the increase of the grain size of the thin alloy ribbons (650 °C 10 min) and enhancing the coercivity of the alloy with Nb addition. It can be seen that Nb enters into the amorphous structure and $\text{Nd}_2\text{Fe}_{14}\text{B}$ phase, which is a

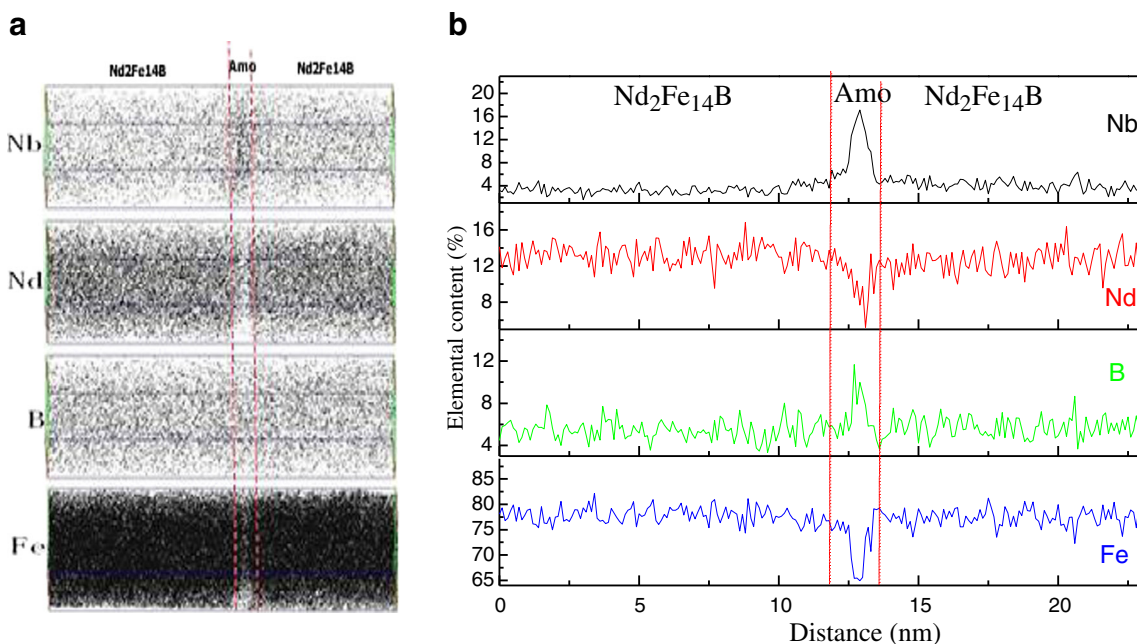


Fig. 7 3DAP analysis results for $\text{Nd}_{12.3}\text{Fe}_{79.2}\text{Nb}_{2.5}\text{B}_{6.0}$ as-spun ribbon at a speed of 22 m/s. **a** Elemental map, **b** the corresponding concentration depth profiles ($8 \times 8 \times 22 \text{ nm}^3$)

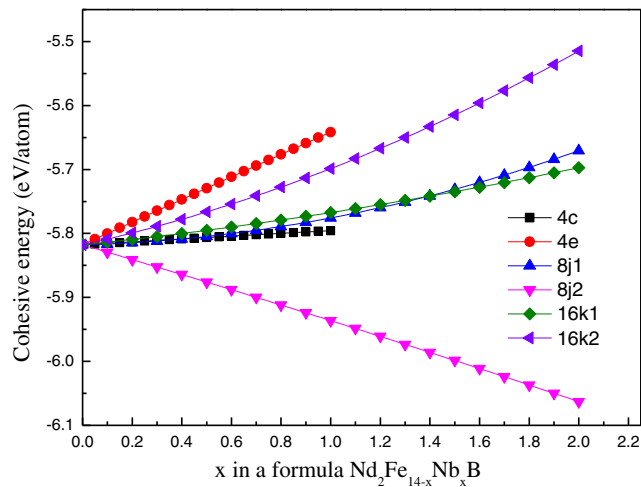


Fig. 8 Cohesive energy and tolerance of $\text{Nd}_2\text{Fe}_{14-x}\text{Nb}_x\text{B}$

little different from nanocomposite $\text{Nd}_2\text{Fe}_{14}\text{B}/\alpha\text{-Fe}$ [22]. In $\text{Fe}^3\text{B}/\text{Nd}_2\text{Fe}_{14}\text{B}$, Nb atoms are contained only in the Fe_{23}B_6 phase [20].

Each $\text{Nd}_2\text{Fe}_{14}\text{B}$ unit cell has six crystallographically inequivalent Fe sites, two inequivalent Nd sites, and one B site. The Fe atoms are set at 4c, 4e, $8j_1$, $8j_2$, 16k₁, and 16k₂ sites, respectively. Fe atoms in each site are replaced by Nd atoms with different concentrations. The substitution concentration for 4c, 4e, $8j_1$, and $8j_2$ is up to 100 %, and 50 % for the two k sites. Simulation was conducted by energy minimization, using the conjugate-gradient method with a cutoff radius of potentials of 14 Å. The system used to relax contains 2 2 2 supercell with 544 atoms. We took the average of 20 samples for each substitution concentration.

Figure 8 shows the variations of cohesive average energy with Nb concentration at different sites. It can be seen that Nb substitution of j_2 site causes the cohesive energy to increase, while substitutions of the other five sites cause

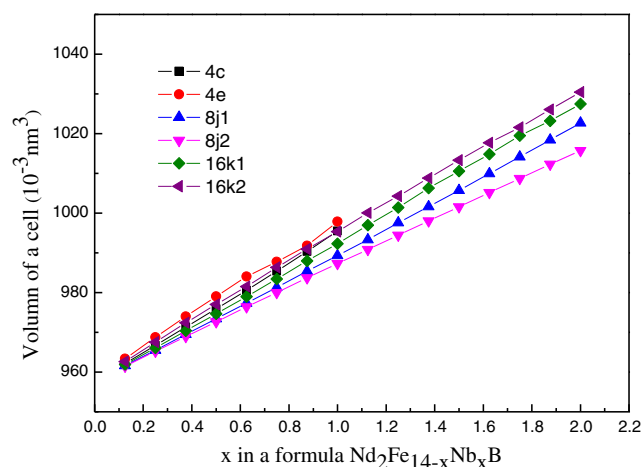


Fig. 9 Cell volume of $\text{Nd}_2\text{Fe}_{14-x}\text{Nb}_x\text{B}$ vs titanium composition x at different sites

the cohesive energy to decrease, indicating that Nb atom will preferentially occupy the $8j_2$ site. There are a few experimental researches about Nb substitution in $\text{Nd}_2\text{Fe}_{14}\text{B}$. Wang et al [11, 12] studied the influence of Nb on $(\text{Nd}_{0.9}\text{Dy}_{0.1})_{9.5}\text{Fe}_{79-x}\text{Co}_5\text{Nb}_x\text{B}_{6.5}$ ($x = 0, 1, 5$) alloy using a three-dimensional atom probe (3DAP). While the concentration of Nb, Fe, and B atoms in Nb-enriched boundary phase became equal, and more Nb atoms were found in $\text{Nd}_2\text{Fe}_{14}\text{B}$ phase [12]. Hui et al [13] believed that Nb should most preferentially replace Fe j_2 site. Although, some researchers found that Nb hardly enter into 2:14:1 phase in nanocomposite magnet material, which was different from $\text{Nd}_2\text{Fe}_{14}\text{B}$ single-phase nanograin.

Figure 9 shows the variations of unit cell volume with different Nb concentration. The covalent radius of Nb (1.34 Å) is larger than Fe (1.17 Å). As Nb increases, the volume of a cell increases. Fe $8j_2$ site has the largest space and Fe 4e site has the smallest space [23]. When the Fe j_2 site is substituted by Nb, the inflation of volume is the least, while if Nb replaces the Fe 4e site, the substituting atom will cause the crystal inflation enormously. Note that all the sites of the cell volume with substituting concentration are almost linear.

4 Conclusions

In summary, the effect of Nb substitution on the magnetic properties, microstructure, and site preference of melt-spun ribbons $\text{Nd}_{12.3}\text{Fe}_{81.7-x}\text{Nb}_x\text{B}_{6.0}$ ($x = 0-3.0$) has been studied. The addition of Nb refined the microstructure and improved the magnetic properties of nanocomposite magnets. For both the amorphous boundary and the boundary between $\text{Nd}_2\text{Fe}_{14}\text{B}$ grains, no second phase or precipitates were found in the grain boundaries. Optimum magnetic properties with $(\text{BH})_{\text{max}} = 143.1 \text{ kJ/m}^3$, $J_r = 0.94 \text{ T}$, $H_{\text{ci}} = 919.0 \text{ kA/m}$ were achieved by annealing the melt-spun ribbons with $x = 1.5$ at 650 °C for 10 min. Besides, in a single-phase $\text{Nd}_2\text{Fe}_{14}\text{B}$ nanograin, Nb atoms preferentially occupied the $8j_2$ site and the cell volume would inflate least.

Acknowledgments The authors are grateful for W. Q. Liu, Shanghai University for 3DAP. This study is supported by the National Natural Science Foundation of China under Grant (No. 51174030).

References

- Gutfleisch, O., Willard, M.A., Bruck, E., Chen, C.H., Sankar, S.G., Liu, J.P.: *Adv. Mater.* **23**, 821 (2011)
- Wang, C., Chen, J.J., Li, Y., Luo, C.L., Chen, W.Z.: *J. Alloys Compd.* **555**, 16 (2013)
- Jianu, A., Valeanu, M., Lazar, D.P., Lifei, F., Bunescu, C., Pop, V.: *J. Magn. Magn. Mater.* **272**, 1493 (2004)

4. Wu, Q., Yu, T., Guo, S., Feng, X.C., Pan, M.X., Zhang, P.Y., Han, B.S., Ge, H.L., Yan, A.R.: *J. Appl. Phys.* **111**, 07A730 (2012)
5. Liu, Z., Lin, W.C., Shih, C.W., Hsieh, C.C., Chang, H.W., Chang, W.C., Yan, A.R.: *J. Alloys Compd.* **538**, 28 (2012)
6. Chang, H.W., Lin, W.C., Shih, C.W., Hsieh, C.C., Chang, W.C.: *J. Alloys Compd.* **545**, 231 (2012)
7. Chen, Z.M., Wu, Y.Q., Kramer, M.J., Smith, B.R., Ma, B.M., Huang, M.Q.: *J. Magn. Magn. Mater.* **286**, 105 (2004)
8. Konno, T.J., Uehara, M., Hirosawa, S., Sumiyama, K., Suzuki, K.: *J. Alloys Compd.* **268**, 278 (1998)
9. Yamasaki, M., Hamano, M., Mizuguchi, H., Kobayashi, T., Hono, K., Yamamoto, H., Inoue, A.: *Scripta Mater.* **144**, 137 (2001)
10. Chen, Z.M., Zhang, Y., Ding, Y.Q., Hadjipanayis, G.C., Chen, Q., Ma, B.M.: *J. Magn. Magn. Mater.* **195**, 420 (1999)
11. Wang, Z.Y., Liu, W.Q., Zhou, B.X., Ni, J.S., Xu, H., Li, Q.: *Rare Met.* **27**, 299 (2008)
12. Wang, Z.Y., Liu, W.Q., Zhou, B.X., Ni, J.S., Xu, H., Fang, Y.Z., Jin, M.L.: *Phys. B* **404**, 1321 (2009)
13. Wang, H.Y., Zhao, F.A., Chen, N.X., Liu, G.: *J. Magn. Magn. Mater.* **295**, 219 (2005)
14. Carlsson, A.E., Gelatt, Jr., C.D., Ehrenreich, H.: *Philos. Mag. A* **41**, 241 (1980)
15. Chen, N.X., Chen, Z.D., Wei, Y.C.: *Phys. Rev. E* **55**, R5 (1997)
16. Chen, N.X., Ren, G.B.: *Phys. Rev. B* **45**, 8177 (1992)
17. Cao, L.Z., Shen, J., Chen, N.X.: *J. Alloys Compd.* **336**, 18 (2002)
18. Qian, P., Wang, Q.L., Chen, N.X., Shen, J.: *J. Phys. D: Appl. Phys.* **39**, 1197 (2006)
19. Xie, G.Z., Wu, Y.P., Lin, Y., Wang, Z.H., Lin, P.H., Gu, B.X., Du, Y.W.: *J. Non-Cryst. Solids* **352**, 2137 (2006)
20. Ping, D.H., Hono, K., Kanekiyo, H., Hirosawa, S.: *IEEE T. Magn.* **35**, 3262 (1999)
21. Zhang, W., Matsushita, M., Inoue, A.: *J. Appl. Phys.* **89**, 429 (2001)
22. Wu, Y.Q., Ping, D.H., Hono, K., Inoue, A.: *IEEE T. Magn.* **35**, 3295 (1999)
23. Givord, D., Li, H.S., Moreau, J.M.: *Solid State Commun.* **50**, 497 (1984)